Quantitative Analysis of Polarization-Controlled Tip-Enhanced Raman Imaging through the Evaluation of the Tip Dipole

Toshihiro Mino, Yuika Saito,* and Prabhat Verma

Department of Applied Physics, Osaka University, 2-1 Yamadaoka, Suita, Osaka, 565-0871 Japan

ABSTRACT Polarization analysis in tip-enhanced Raman spectroscopy (TERS) is of tremendous advantage, as it allows one to study highly directional intrinsic properties of a sample at the nanoscale. However, neither evaluation nor control of the polarization properties of near-field light in TERS is as straightforward as in usual far-field illumination, because of the random metallic nanostructure attached to the tip apex. In this study, we have developed a method to successfully analyze the polarization of near-field light in TERS from the scattering pattern produced by the induced dipole in the metallic tip. Under dipole approximation, we measured the image of the dipole at a plane away from the focal plane, where the information about the direction of the dipole oscillation was intact. The direction of the dipole oscillation was determined from the defocused pattern, and then the polarization of near-field light was evaluated from the oscillation direction by calculating the intensity distribution of near-field light through Green's function. After evaluating the polarization of some fabricated tips, we used those tips to measure TERS images from single-walled carbon nanotubes and confirmed that the contrast of the TERS image depended on the oscillation direction of the dipole, which were also found in excellent agreement with the calculated TERS images, verifying that the polarization of the near-field was quantitatively estimated by our technique. Our technique would lead to better quantitative analysis in TERS imaging with consideration of polarization impact, giving a better understanding of the behavior of nanomaterials.

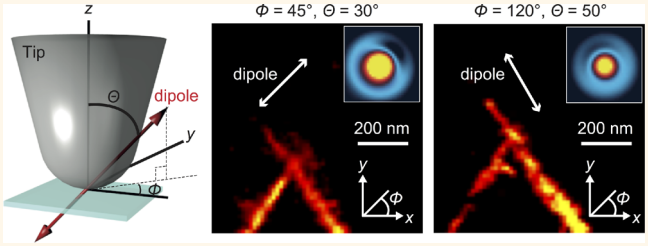

KEYWORDS: polarization · near-field · tip-enhanced Raman spectroscopy · defocused imaging · plasmon · nanoimaging

Many intrinsic properties of commonly used samples are extremely sensitive to the polarization of the illumination light. An optical imaging technique based on polarization-controlled illumination can therefore be a valuable tool to study distinct properties of a sample. One of the most prevailing optical techniques is Raman spectroscopy, which can also be used as scanning microscopy for imaging purposes. If the polarization of the illumination light in Raman measurements is precisely controlled, one can selectively excite different Raman modes that are sensitive to the illumination polarization. Therefore, when Raman microscopy is combined with polarization-controlled illumination, it is possible to reveal unique characteristics of samples, such as molecular symmetries, orientations, and intermolecular interactions. Such polarization-controlled Raman (*p*-Raman) microscopy has been used in the past for crystallography,[1,2] polymer analysis,[3] and observation of biological processes.[4] However, due to the diffraction limit of light, the spatial resolution of this imaging technique is restricted at best to about 300 nm in the visible range. Recent development of nanoscale science and technology, where a tiny difference in molecular orientation can be of great importance, is boosting interest in *p*-Raman imaging at higher resolution. With recent technological advances, the devices are becoming smaller and smaller, which makes it even more challenging to characterize these devices at the nanoscale and thereby control their performances. For example, thin films of pentacene molecules are often used to produce organic transistors. Pentacene is a tall molecule that should ideally attach perpendicularly to the substrate to

* Address correspondence to yuika@ap.eng.osaka-u.ac.jp.

Received for review June 12, 2014 and accepted August 29, 2014.

Published online August 29, 2014
10.1021/nn5031803

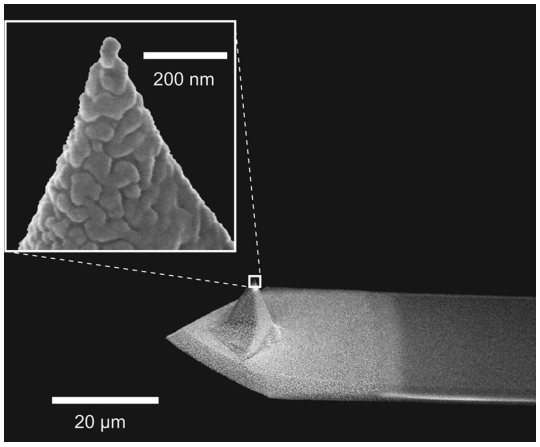

Figure 1. SEM image of a metallic tip made by evaporating Ag on a silicon cantilever for AFM. The inset shows random Ag nanostructures at and around the tip apex.

make this thin film. However, very often these molecules randomly tilt within small islands of 10−100 nm size.[2] This variation in molecular tilt can greatly affect the carrier mobility, and therefore it is very important to identify the tilt angles. No existing techniques, such as X-ray scattering or micro-Raman spectroscopy, can identify such localized variation in molecular orientation. On the other hand, polarization-controlled tip-enhanced Raman spectroscopy (*p*-TERS), which has a spatial resolution of 10−20 nm and is capable of sensing the molecular orientation, can produce nanoimages of the sample showing variations of molecular orientation at the nanoscale. This would be of huge advantage to improve and control the performances of organic devices.

As of now, TERS is the only technique that can realize Raman measurements at extremely high spatial resolution, far beyond the diffraction limit of light.[5−12] TERS utilizes a metallic nanotip that is approached to the sample in the focus spot of illuminated light. Owing to the resonant excitation of the localized surface plasmon polaritons (LSPPs) at the tip apex, a strongly enhanced and highly confined light field is created in close proximity to the tip apex, which provides super-high spatial resolution in TERS measurement. Several samples, such as DNA molecules,[13] silicon devices,[14] single-walled carbon nanotubes (SWNTs),[15−19] and graphene,[20,21] have been studied by TERS at high spatial resolution, and attractive information at the nanoscale has been reported from these samples. However, there are no reports so far on polarization-controlled TERS. The polarization of incident light in TERS, which is essentially the evanescent light confined at the tip apex, is not as simple as that in conventional Raman spectroscopy due to the depolarization effect inherently produced by the metallic tip.[22,23] This can be qualitatively understood from the scanning electron microscopy (SEM) image in Figure 1, which shows the structure of evaporated metal on a commonly used AFM-based TERS tip. This tip was prepared by evaporating silver on a silicon cantilever used in contact-mode AFM. The zoomed image in the inset shows randomly grown silver nanoparticles near as well as on the apex of the tip. These random nanoparticles that generate and thus control the behavior of the confined light are truly random, as no existing fabrication techniques can precisely control the shape, size, and orientation of these metal structures with high accuracy. Since all properties of near-field light, such as polarization, spatial resolution, and enhancement factor, depend on the geometry of the metallic nanostructure at the apex of the tip, the actual polarization of near-field light for a commonly used tip remains ambiguous. The best deal in such a situation could be to precisely determine the polarization of near-field light for a given tip and then utilize this information for measuring *p*-TERS from a sample. However, there currently exists no experimental method to determine the status of near-field polarization for a given tip.

The TERS system used in the present study was an AFM-based system. However, STM-based TERS systems are also equally popular.[12,24] The main difference between the two systems is the tip. In AFM-based TERS, we often use a commercially available silicon cantilever, which is covered with evaporated silver metal. This forms a thin and rough layer of silver on the tip with grain size typically varying from 20 to 50 nm. These tips usually have a silver nanoparticle at the apex, and several similar nanoparticles covering the entire tip surface (Figure 1). These tips cannot be geometrically reproduced due to the randomness in the shapes and sizes of the evaporated nanoparticles. However, the average plasmonic properties can still be reproduced. Due to the random nature of the shape and size of the evaporated silver nanoparticles, particularly the particle at the apex of the tip, the polarization of the near-field light generated at the apex is also random with extreme variations, even when the tips are fabricated under identical conditions. This gives us a possibility to have varied polarizations from tip to tip, which can be readily utilized in *p*-TERS measurements. On the other hand, the tips used in STM-based TERS are made of solid metal, usually gold, and have a very smooth surface with a sharp apex. These tips are comparatively easily reproducible, because they have regular geometry. Due to their smooth surfaces and regular shapes, the STM-based tips generate near-field light with stronger *z*-polarization, which does not have much variation from tip to tip, when the tips are produced under identical conditions. We believe that AFM-based tips are better for *p*-TERS measurements with wider variations in near-field polarization, as compared with the STM-based tips. Nevertheless, it would still be interesting to compare *p*-TERS for the two different configurations.

In this work, we have developed an experimental method to precisely evaluate the polarization of the near-field light confined at the apex of a given metal-coated TERS tip. This is done with the assistance of theoretical simulation, which is compared to the experimental result to estimate the exact polarization at the tip apex. We assumed that when a metal-coated tip with a nanoparticle attached to the tip apex, as in the inset of Figure 1, is illuminated by a resonant light, only a dipolar plasmon is excited at the tip apex. This assumption is reasonable because the tip apex (about 30 nm in radius) is small enough compared with the wavelength of the incident light (488 nm). Here, we would like to clarify that the tip apex in our experiment was illuminated under total internal reflection, where the propagating light is reflected back and only evanescent light exists on the tip side. The decay length of evanescent light is about 50−60 nm; thus only the nanoparticle at the tip apex is effectively illuminated. It is therefore reasonable to consider that only a dipolar plasmon is excited at the tip apex. In such cases, the oscillation direction of the dipole at the tip apex determines the polarization of the near-field light around the tip apex. One can best evaluate the tip by measuring its scattering pattern, since this allows one to distinguish the dipolar plasmon from the other multipolar plasmons.[25,26] The oscillation direction of the dipole is determined from the asymmetry in the scattering pattern.[27,28] The light emitted from a dipole in the direction perpendicular to the dipole oscillation is stronger than the light emitted in the parallel direction, which provides asymmetry to the scanning pattern. The directional information is, however, lost when the emitted light is well focused in order to form an image of the dipole. Nevertheless, one can still find this information intact at a plane away from the focal plane. Therefore, a technique known as defocused imaging is perfect for analyzing the scattering pattern, and it has been used in the past to investigate the orientations of fluorescent molecules.[29] Here we investigate the oscillation direction of the dipole at the apex of a metallic tip by using the defocused imaging technique and analyze the polarization of the near-field light around the tip apex from this oscillation direction by estimating the intensity distribution through Green's function.

Some authors in the past have used the back focal plane imaging technique to measure the dipole orientation in fluorescent molecules,[30−32] coupled metal nanoparticles,[33] and carbon nanotube.[34] By measuring near-field photoluminescence from carbon nanotubes,[34] the authors observed the angular radiation pattern and argued that the radiative rate enhancement is connected to the directional redistribution of the emission. Back focal plane imaging has an advantage over defocused imaging when the dipole is in-plane-oriented.[30] Moreover, in back focal imaging, the emission pattern is directly recorded in the exit pupil of an optical system, which makes the method less sensitive to phase aberration and independent of knowledge of the amount of defocus.[30] On the other hand, in our experiments, the *z*-component is dominant in the dipole due to the high sensitivity of the tip to *z*-polarization.[35] Moreover, we detect Rayleigh scattering light from the tip, where speckle noise reduces the accuracy of the determination of the dipole orientation by back focal plane imaging. For these reasons, we believe that the defocused imaging is better for our present experimental configuration, and hence we utilized this technique rather than the back focal plane imaging.

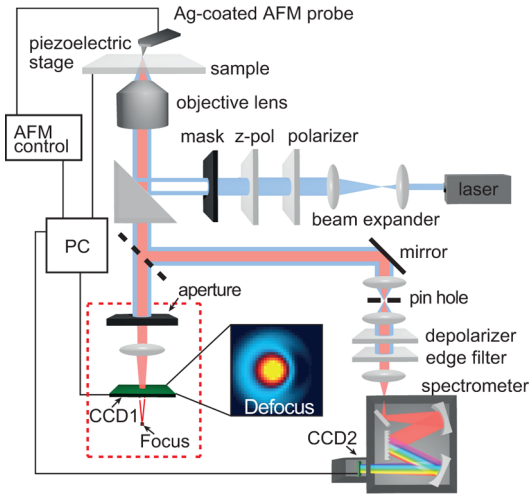

Figure 2. Experimental setup for defocused imaging and TERS measurements. The part used for defocused imaging is enclosed by the red dotted line. After the aperture rejected components with NA > 0.64, the beam diameter in the collimated light path was 4 mm. A defocused image was obtained by detecting the scattered light through a lens of focal length 200 mm and CCD1 positioned 3 mm away from the focal plane.

RESULTS AND DISCUSSION

Figure 2 shows a schematic diagram of our experimental setup. Here, we modified the commonly used TERS microscopy system by incorporating some optics for defocused imaging. Unlike the fluorescence defocused imaging, where the sample is illuminated by a defocused light *via* a defocused objective lens, in our experiment, the tip apex is illuminated with a tightly focused light, while the image of the tip dipole is defocused on the detector, as shown by the area enclosed in the red dotted line in Figure 2. The benefit of this setup is that we could obtain a defocused pattern of the dipole scattering image, while keeping the laser light focused on the tip apex, which is necessary for efficient excitation of the near-field light at the tip apex.

Theoretical Simulation of Defocused Dipole Patterns. In order to properly understand and evaluate the asymmetry of the defocused images in our experiments, we first performed numerical calculations to simulate

defocused image patterns in various possible conditions. The calculation procedure is summarized in the Methods section. Figure 3 shows such calculated defocused image patterns for several dipole orientations. As one can see from these calculated dipole scattering images, the intensity distribution in the defocused pattern changes with the direction of the dipole oscillation. Here, we defined the $x-y$ plane as the sample plane and the z-axis as the propagation direction of the incident light (perpendicular to the sample plane). The direction of the dipole oscillation (represented by vector D) is described by a tilt angle Θ and a twist angle Φ. The tilt angle Θ is the angle between the dipole axis and the z-axis, and the twist angle Φ is the angle between the x-axis and the in-plane component of the dipole ($D_x + D_y$). When the dipole is in the z-direction ($\Theta = 0°$), the defocused pattern shows a doughnut shape with a dark center (Figure 3b). As Θ increases, the central dark area moves to the side and a crescent-shaped dark structure appears at one side of the outer ring (Figure 3c). We can estimate the dipole orientation (Θ and Φ) from the size and the position of this dark crescent. The larger the Θ value is, the smaller the size of the crescent becomes (Figure 3c → d). Further, the position of the crescent depends on the twist angle, and it moves in the direction indicated by Φ (Figure 3d → e → f). We can quantitatively determine Θ and Φ from the size and the location of the dark crescent by using an algorithm based on the least-squares method reported in the literature.[36]

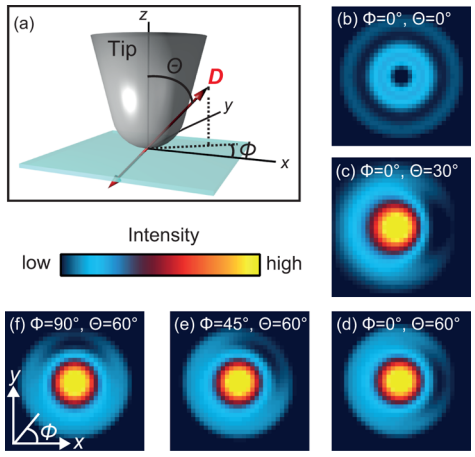

Figure 3. (a) Schematic diagram of the spatial coordinate system at the tip apex and the definition of tilt and twist angles (Θ, Φ) for the dipole orientation D. (b–f) Calculated defocused image patterns for various dipole orientations.

Experimental Measurements of Defocused Dipole Patterns. Our defocused image measurement technique clearly shows unique patterns for different tips. In fact, even when the tips are prepared under identical experimental conditions, they showed different patterns in the defocused images, indicating that the polarization properties varied from tip to tip. In order to understand this, we selected three different tips prepared under identical conditions (here we call them Tip1, Tip2, and Tip3), SEM images of which are shown in Figure 4a–c. Experimental defocused scattering patterns of the three tips are shown in Figure 4d–f. The dark crescents could be observed in the defocused patterns, which indicates that the dipole excited at the apex of these metallic tips was tilted and twisted relative to the z-axis, although the excitation polarization was in the z-direction (perpendicular to the plane of the substrate) in all the measurements. We calculated the best fitted values of Θ and Φ for each tip by comparing the experimental defocused patterns with the calculated defocused patterns using the least-squares method. The best fitted values for the tilt and twist angles were quantitatively determined to be $\Theta = 30°$ and $\Phi = 45°$ for Tip1, $\Theta = 40°$ and $\Phi = 90°$ for Tip2, and $\Theta = 50°$ and $\Phi = 120°$ for Tip3. The error in both Θ and Φ is estimated to be $\pm 5°$ for all tips. Clearly, the directions of the dipole oscillations were different for the three tips even when they were fabricated under identical experimental conditions, indicating that the polarization of near-field light is expected to depend on the tip used in a measurement. This variation in the

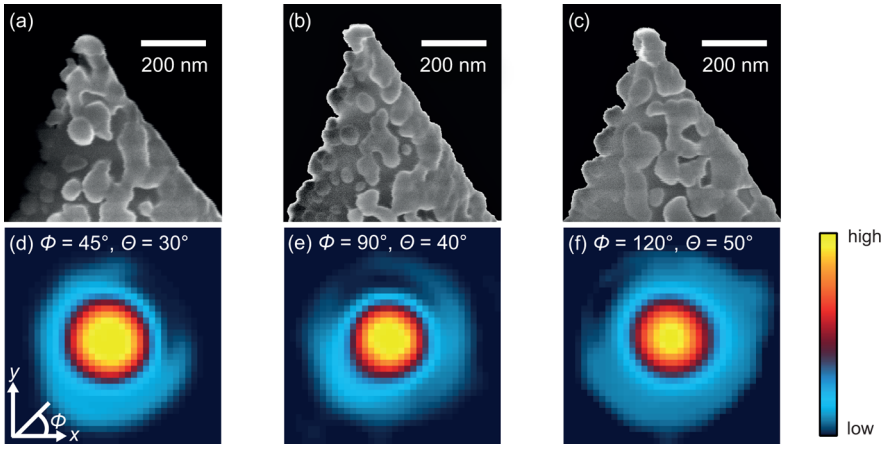

Figure 4. SEM images of Tip1 (a), Tip2 (b), and Tip3 (c). Experimental defocused patterns of the scattering light from Tip1 (d), Tip2 (e), and Tip3 (f). The errors in both Θ and Φ are approximately $\pm 5°$ for all tips.

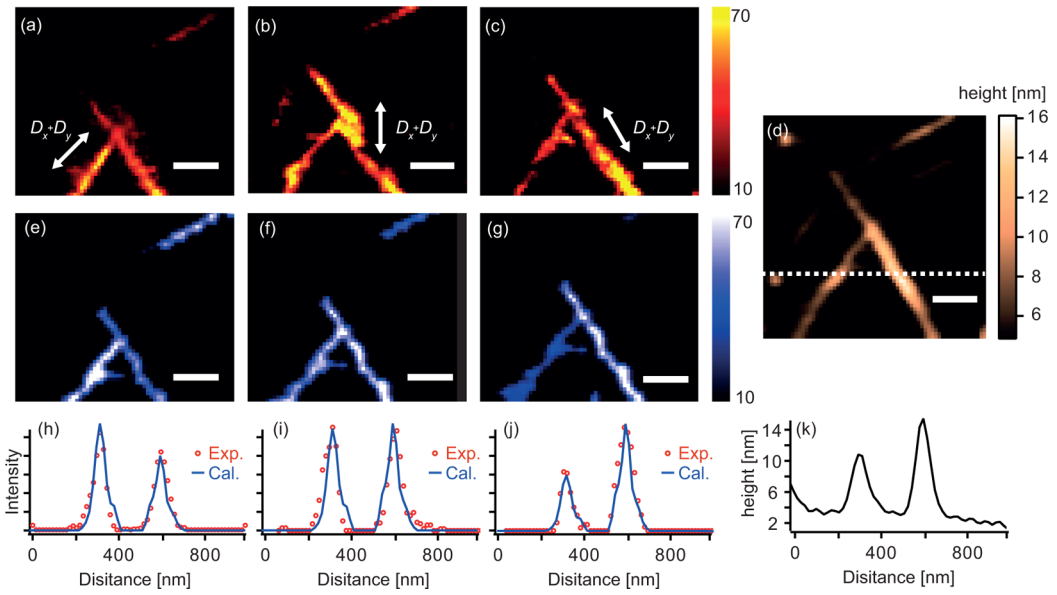

Figure 5. (a−c) TERS images of SWNTs taken by Tip1 (a), Tip2 (b), and Tip3 (c). The white arrows in the images show the in-plane components of the dipole, $D_x + D_y$. (d) AFM image at the sample. (e−g) Calculated TERS images in the cases where Tip1 (e), Tip2 (f), and Tip3 (g) were used to observe the SWNTs. (h−j) Line profiles of the experimental (red open circles) and the calculated (blue solid lines) TERS images along the white dotted line shown in the AFM image for Tip1 (h), Tip2 (i), and Tip3 (j). All scale bars in the images are 200 nm.

polarization properties of the tips was caused by the randomness of the metallic structure attached to the tip apex, as one can also see in the SEM images. During the evaporation of Ag on the tip, the Ag particles grow at random positions with random sizes and shapes around the apex of the tip. It is not possible to estimate the polarization property of the tip just by looking at these metallic structures from the SEM images, which suggests that the relationship between the polarization properties and the metal structures is not straightforward. A slight change in the positions and the shapes of Ag particles attached to the tip apex would dramatically affect the polarization properties. Moreover, even when we use the same metallic tip, the orientation of the dipole excited at the apex could change depending upon the position of the tip apex inside the tightly focused laser spot, where the excitation polarization is not uniform. This result supports the reported polarization-dependence of TERS spectra, where samples were illuminated with light having varied polarizations.[37,38] Further, the dipole orientation depends on the tilt angle of the cantilever as well. Since the direction of the dipole oscillation at the apex of a tip is not predictable from the fabrication procedure or from the SEM image of the metallic structure at the tip, defocused imaging is an indispensable technique to determine the direction of the dipole oscillation for each tip used in every measurement. Once the dipole direction is correctly determined for a given tip, it can be utilized for the near-field polarization-dependent studies for various applications.

TERS Experiments. In order to demonstrate that the polarization of the near-field probe can be correctly estimated from the direction of the dipole oscillation, we performed TERS measurements on SWNTs by using the tips that were already evaluated for their dipole orientation through the defocused imaging technique. Since the transition moment of the G^+-band in the Raman spectrum of SWNTs under resonant conditions is known to be parallel to the long axis of the SWNT,[39] the contrast of a G^+-band intensity image can be predicted by the polarization state and the molecular orientation, which can be easily determined from a topographic image. Therefore, a SWNT is one of the most suitable samples for our demonstration. As a dipole produces strong polarization in the direction of its oscillation, the SWNTs oriented in the dipole direction should exhibit strong G^+-band intensity. We can therefore confirm the estimated values of Θ and Φ for our near-field probe.

Figure 5a−c show TERS images, constructed from the intensity of the G^+-band of SWNTs, in the neighboring area taken with Tips1−3 (Figure 4), respectively. The sample contained some bundled SWNTs in various orientations. An AFM topographic image taken from the same sample area is also shown in Figure 5d. As estimated from the height in the AFM image, a few tens of SWNTs were bundled together. Before measuring TERS images, we confirmed that the defocused pattern of the dipole was not affected by the presence of the sample, which indicated that the sample with a few tens of SWNTs was thin enough compared with the metallic tip to affect the orientation of the tip dipole. The white arrows in Figure 5a−c indicate the in-plane components of the dipoles ($D_x + D_y$), represented by the twist angles Φ, excited at the tip apex. Due to the

tight focusing of incident light *via* the high-NA objective, the incident polarization is usually not uniform within the focus spot. However, since the position of the tip is locked with respect to the focus spot and only samples are scanned during imaging, the variation of incident polarization within the focus spot does not affect the TERS image.

As expected, the intensity variation in TERS images of the sample clearly shows that the polarizations parallel to the dipole orientation are dominantly excited. One can see that the SWNTs oriented in the direction parallel to the white arrows have a larger intensity compared to the SWNTs in the perpendicular direction. In Figure 5a, the G^+-band intensity from the left lower arm of the sample was stronger than that from the other arm. In contrast, the right arm of the sample was preferentially excited in Figure 5c, where the excited dipole was parallel to that arm. Both arms of the sample were observed with almost the same intensity in Figure 5b. Moreover, the SWNTs present in the upper-right area of the AFM image were observed in Figure 5a and b, but were not observed in Figure 5c, as it is oriented perpendicular to the dipole in Figure 5c. One can notice in Figure 5b that the nanotube bundle seems to show a discontinuity around the center. This is probably some artifact, which might have been caused by temporary fluctuation of some experimental condition. However, since this minor imperfection does not affect our result and analysis, we ignore it in further discussions.

In order to have a quantitative evaluation of the near-field polarization, we present a comparison of experimental TERS images with the corresponding calculated TERS images, as shown in Figure 5e–g. We calculated the TERS images by following two enhancement mechanisms, commonly discussed in the past for surface-enhanced Raman spectroscopy (SERS).[40,41] In the first mechanism, the sample is illuminated with strongly confined near-field light generated by the dipole induced at the apex of a metallic tip. The light field generated by the dipole was calculated by using Green's function, as discussed in previous work.[42,43] In the second mechanism, near-field light around the sample is scattered by the metallic tip, and this is detected as a TERS signal. In this scattering mechanism, near-field light polarized in the direction indicated by the dipole at the tip apex is preferentially scattered, because such near-field light induces a strong dipole oscillation at the tip apex. The intensity of the TERS signal can thus be calculated from the direction of the dipole oscillation. As one can see, the calculated images are very similar to the experimental images, particularly in terms of the contrast between the arms of the SWNT sample. To make the similarity between the experimental and the calculated TERS images more obvious, Figure 5h–j display the line profiles of the TERS images along the white dotted line shown in Figure 5d. For a comparison, the line profile of the AFM image is also shown in Figure 5k. The line profiles of the TERS images show that the experimental results, indicated by the red open circles, are in excellent agreement with the calculated results, indicated by the blue solid line. This confirms that we can precisely analyze the polarization of near-field light from the direction of the dipole oscillation. The revealed polarization of near-field light is utilizable to perform polarization analysis in TERS and to obtain molecular orientations and interactions of a sample at the nanoscale.

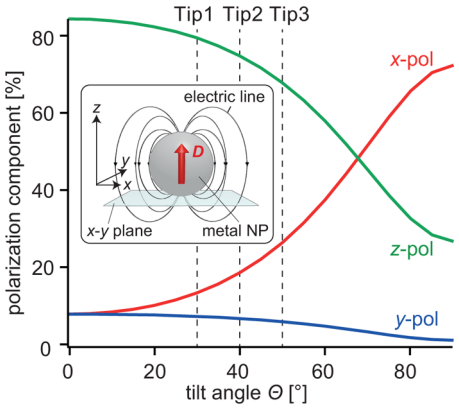

Figure 6. Polarization components of near-field light against the tilt angle Θ of the dipole for the twist angle Φ = 0°. The inset shows the electric line around a metal particle generated by the dipole oscillating in the *z*-direction.

Far-field Raman imaging with linearly polarized light usually shows strong contrast for excitations in two perpendicular polarizations.[39,44] However, as we see from Figure 5a and c, the polarization contrast for the near-field light in the *x*–*y* plane is low. This is because the dipole oscillating in the *z*-direction generates not only *z*-polarization but also both *x*- and *y*-polarizations, as shown in the inset of Figure 6, where the electric line represents the polarization of near-field light. The intensities of the *x*- and *y*-polarizations generated by the dipole in the *z*-direction, where both Θ and Φ = 0°, are the same. The dipole at the apex of the metallic tip always has a certain amount of *z*-component, which makes both *x*- and *y*-polarization nonzero. Figure 6 shows the calculated results of polarization components against the tilt angle Θ, where we assumed a constant value of the twist angle Φ = 0°. The black dotted lines marked with Tip1, Tip2, or Tip3 in Figure 6 indicate the Θ values of the dipoles for Tip1, Tip2, and Tip3, respectively. The calculation was performed within a 30 nm × 30 nm square area in the *x*–*y* plane at a distance of 1 nm away from the tip apex in the *z*-direction by using Green's function (see Methods). The polarization contrast in the *x*–*y* plane increases with an increase in Θ, and when the dipole is perfectly oriented in the *x*-direction (Θ = 90° and Φ = 0°), the *x*- and *y*-polarization components become 71% and 1%, respectively, although such a dipole oscillation does not occur in practice due to the tip

structure, which is more sensitive to *z*-polarization than the *x*- or *y*-polarizations. Near-field light around the apex of the metallic tip is not perfectly polarized in a single direction, and therefore, the polarization behavior in TERS is essentially different from that in conventional polarization Raman spectroscopy.

We would also like to consider the contrast between *z*-polarization and the polarization component in the *x*−*y* plane. As seen from the calculated results in Figure 6, the *z*-polarization is at least twice as strong as the polarization component in the *x*−*y* plane for the experimentally observed range of the tilt angle Θ. The polarization state of near-field light around the apex of a metallic tip has been theoretically discussed in the past with a simple model,[43] which also suggests that the polarization of near-field light in the *z*-direction should be stronger. The high *z*-sensitivity of the near-field polarization is an advantage of TERS and can be applied to the measurements of samples with linear molecules, such as the pentacene thin film, where the molecular orientation on a substrate plays an important role in determining the electronic properties of the sample. The polarization-dependent TERS imaging would reveal the nanoscale difference in molecular orientation, which would be of great importance in future device applications.

CONCLUSION

We quantitatively evaluated the polarization of near-field light in TERS by measuring the scattering pattern produced by a metallic tip using the technique of defocused imaging, which determines the direction of the dipole oscillation at the tip apex and therefore the polarization of near-field light. Our technique demonstrates a direct method to evaluate the tip dipole and the near-field polarization of a given tip. We conclude that investigation of the near-field polarization of individual tips is necessary, because metallic tips have their own unique polarization properties even if they are prepared under identical conditions. The success of our technique was confirmed from TERS images of SWNTs, where near-field polarization dependence was observed as compared with theoretically calculated images. The SWNTs oriented in the direction of a dipole oscillation were strongly excited, which indicated that the tip dipole generated dominant polarization in its oscillation direction. The experimentally obtained TERS images were successfully reproduced from the direction of the dipole oscillation *via* a numerical calculation. This ensured the quantitative performance of our polarization evaluation. We discussed the polarization contrast of near-field light as well. The linear polarization entirely in either the *x*- or *y*-direction is not found in TERS because of the high percentage of the *z*-polarization component. For this reason, the evaluation of the dipole oscillation is all the more necessary to obtain the precise state of the near-field polarization. Polarization-resolved TERS can be achieved without the linear polarization by taking into account the state of the dipole formed at the metallic tip. The revealed polarization of near-field light provides not only unique information such as nanoscopic molecular orientations and intermolecular interactions of a sample, but also quantitative interpretation of TERS images, showing the potential of TERS imaging to contribute to nanoscience in the future.

METHODS

Experimental Setup. An illustration of the optical setup is shown in Figure 2. The system is based on a transmission-mode TERS setup described elsewhere.[45] We generated radially polarized light (wavelength: 488 nm) for a strong longitudinal field by using an eight-segmented half-wave plate (Nanophoton Inc., Z-pol). The optical components used for defocused imaging are shown in the area enclosed by the dotted line. The aperture allows the scattered components in the range NA < 0.64 from the tip to pass and rejects the reflected components of the incident light. A defocused image was measured by a charge coupled device (CCD) camera, CCD1, positioned 3 mm away from the focus plane. In TERS measurements, Raman scattering light was directed to a spectrometer, which was then detected by a liquid-nitrogen-cooled CCD (CCD2).

The TERS measurements shown in Figure 5 were performed in a 1000 nm × 860 nm area, with 64 × 55 pixels. The power of the incident laser light at the sample was 150 μW, and the exposure time at each point was 0.4 s. First, a near-field image was obtained by approaching a metallic tip to the sample, and then a far-field image was obtained by retracting the tip. A pure near-field image was constructed by subtracting the far-field signal from the near-field signal.

The metallic tips were prepared from commercially available silicon cantilevers used in contact-mode AFM. By following the procedure described in detail in the literature,[46] we oxidized the tip for 1.5 h and deposited a 60 nm thick silver layer by vacuum evaporation at a rate of 0.5 Å/s. The radius of the tip apex in our experiments was about 30−40 nm, as estimated from the SEM images.

In order to prepare our SWNT samples, we dissolved the commercially purchased SWNTs in 1,2-dichloroethane through a 30 min sonication. The solution was left for 1 h to extract the supernatant. The supernatant was again diluted with the same solvent and was sonicated for 1 h. The solution was dropped on a cover glass heated by a hot plate to fix the sample on the substrate to avoid dragging during the TERS measurements.

Computational Procedures. The defocused image pattern was calculated from the oscillation direction of a dipole $\mathbf{D}(\Theta_{Tip},\Phi_{Tip})$, where Θ_{Tip} is the tilt angle and Φ_{Tip} is the twist angle of the tip dipole. First, the electric field of the scattering light propagating in a direction $\mathbf{P}(\theta,\varphi)$, where θ represents the tilt angle and φ represents the twist angle of the propagation direction, is described as $\mathbf{P}(\theta,\varphi) \times \mathbf{D}(\Theta_{Tip},\Phi_{Tip}) \times \mathbf{P}(\theta,\varphi)$. By using this formula, the scattering pattern of the dipole before the objective lens was calculated. Modifying the scattering pattern with the rotation matrix $\mathbf{R}(\theta,\varphi)$, we obtained the electric field pattern after the objective lens. More details of the above procedures can be found in the literature.[27] A defocused pattern was then calculated from the electric field pattern after the objective lens by using the Richards and Wolf vectorial diffraction method.[47] In order to keep the calculation realistic, we assumed that the focal length of the lens used for defocused imaging was 200 mm, the diameter of the aperture

was 4 mm, and the image was obtained at a plane 3 mm away from the focal plane.

The model for the calculation of near-field light is described below. We assumed that the tip apex was an Ag nanoparticle with a 30 nm radius. A tip dipole $\mathbf{D}_{Tip}(\Theta_{Tip},\Phi_{Tip})$ was placed at the position $\mathbf{r}$, which was identical to the center of the nanoparticle. We calculated the electric field $\mathbf{E}_{Loc}(\mathbf{r}')$ at position $\mathbf{r}'$ within a plane 1 nm away from the surface of the nanoparticles by using Green's function, G^0:

$$\mathbf{E}_{Loc}(\mathbf{r}') = \frac{\omega^2}{\varepsilon_0 c^2} G^{\circ}(\mathbf{r},\mathbf{r}')\cdot\mathbf{D}_{Tip}(\Theta_{Tip},\Phi_{Tip}) \quad (1)$$

Here ω is the light frequency, ε_0 is the permittivity of the vacuum, and c is the speed of light in a vacuum. As mentioned before, two enhancement mechanisms were considered for calculating the TERS images. In the first mechanism, SWNTs are excited by the electric field $\mathbf{E}_{Loc}(\mathbf{r}')$ in the vicinity of a metallic tip. The excited Raman dipole $\mathbf{D}_{NT}$ is represented by

$$\mathbf{D}_{NT} = \alpha_{NT}\mathbf{E}_{Loc}(\mathbf{r}') \quad (2)$$

where α_{NT} denotes the Raman tensor of the SWNTs. In the second mechanism, the dipole $\mathbf{D}_{NT}$ is amplified by the metallic tip and creates a dipole $\mathbf{D}'_{Tip}$. We can calculate the electric field $\mathbf{E}'_{Loc}$ around the SWNTs by substituting $\mathbf{D}_{Tip}$ into eq 1 with $\mathbf{D}_{NT}(\Theta_{NT}, \Phi_{NT})$ where Θ_{NT} is the tilt angle and Φ_{NT} is the twist angle of the SWNTs. The dipole $\mathbf{D}'_{Tip}$ excited by the electric field $\mathbf{E}'_{Loc}$ is expressed by

$$\mathbf{D}'_{Tip}(\Theta_{Tip},\Phi_{Tip}) = \alpha_{Tip}\frac{\omega^2}{\varepsilon_0 c^2} G^{\circ}(\mathbf{r},\mathbf{r}')\cdot\mathbf{D}_{NT}(\Theta_{NT},\Phi_{NT}) \quad (3)$$

where α_{Tip} is the polarizability tensor of the metallic tip. The far-field light scattered from the dipole $\mathbf{D}'_{Tip}$ is then detected. Finally, the detected TERS signal can be calculated from eq 3 by integrating[42] along the nanotube over the area under the tip apex. The signal collection efficiency must also be taken into account.[48] According to the above procedure, we can calculate the TERS image if the polarizability tensor of the metallic tip α_{Tip} and the Raman tensor of the SWNTs α_{NT} are known. The polarizability tensor of the metallic tip and the Raman tensor of the SWNTs were determined from the orientation of the dipole and those of the molecules $(\Theta_{Tip(NT)}, \Phi_{Tip(NT)})$ by using the following rotation matrix $\mathbf{R}$ and the tensor α in the case where the dipole and the long axes of SWNTs are parallel to the z-direction:

$$\alpha_{Tip(NT)} = \mathbf{R}(\Theta_{Tip(NT)}, \Phi_{Tip(NT)})^T \alpha \mathbf{R}(\Theta_{Tip(NT)}, \Phi_{Tip(NT)}) \quad (4)$$

$$\alpha = \begin{pmatrix} 0 & 0 & 0 \\ 0 & 0 & 0 \\ 0 & 0 & A \end{pmatrix}$$

where A is a constant. The orientation of the tip dipole $(\Theta_{Tip}, \Phi_{Tip})$ was determined from the defocused pattern. The tilt angles Θ_{NT} of the SWNTs were defined to be 90° under the assumption that the SWNTs were parallel to the sample plane, and the twist angles Φ_{NT} were determined from the shape of the SWNTs observed in an AFM image.

Conflict of Interest: The authors declare no competing financial interest.

Acknowledgment. The authors would like to acknowledge the financial support from the JSPS Asian Core Program and Grant-in-Aid for Scientific Research (C) 24560028.

Supporting Information Available: Detailed Raman spectra of SWNTs and comparison between experimental and theoretically calculated defocused patterns of a dipole are included. This material is available free of charge *via* the Internet at http://pubs.acs.org.

REFERENCES AND NOTES

1. Ossikovski, R.; Nguyen, Q.; Picardi, G.; Schreiber, J. Determining the Stress Tensor in Strained Semiconductor Structures by Using Polarized Micro-Raman Spectroscopy in Oblique Backscattering Configuration. *J. Appl. Phys.* **2008**, *103*, 093525.
2. Mino, T.; Saito, Y.; Yoshida, H.; Verma, P. Molecular Orientation Analysis of Organic Thin Films by Z-Polarization Raman Microscope. *J. Raman Spectrosc.* **2012**, *43*, 2029–2034.
3. Sourisseau, C. Polarization Measurements in Macro- and Micro-Raman Spectroscopies: Molecular Orientations in Thin Films and Azo-Dye Containing Polymer Systems. *Chem. Rev.* **2004**, *104*, 3851–3891.
4. Harms, G. S.; Sonnleitner, M.; Schutz, G. J.; Gruber, H. J.; Schmidt, T. Single-Molecule Anisotropy Imaging. *Biophys. J.* **1999**, *77*, 2864–2870.
5. Kawata, S.; Inouye, Y.; Verma, P. Plasmonics for Near-Field Nano-Imaging and Superlensing. *Nat. Photonics* **2009**, *3*, 388–394.
6. Verma, P.; Ichimura, T.; Yano, T.; Saito, Y.; Kawata, S. Nano-Imaging through Tip-Enhanced Raman Spectroscopy: Stepping beyond the Classical Limits. *Laser Photonics Rev.* **2010**, *4*, 548–561.
7. Yano, T.; Verma, P.; Saito, Y.; Ichimura, T.; Kawata, S. Pressure-Assisted Tip-Enhanced Raman Imaging at the Resolution of a Few Nanometers. *Nat. Photonics* **2009**, *3*, 473–477.
8. Inouye, Y.; Kawata, S. Near-Field Scanning Optical Microscope with a Metallic Probe Tip. *Opt. Lett.* **1994**, *19*, 159–161.
9. Stockle, R. M.; Suh, Y. D.; Deckert, V.; Zenobi, R. Nanoscale Chemical Analysis by Tip-Enhanced Raman Spectroscopy. *Chem. Phys. Lett.* **2000**, *318*, 131–136.
10. Yu, J.; Saito, Y.; Ichimura, T.; Kawata, S.; Verma, P. Far-Field Free Tapping-Mode Tip-Enhanced Raman Microscopy. *Appl. Phys. Lett.* **2013**, *102*, 123110.
11. Umakoshi, T.; Yano, T.; Saito, Y.; Verma, P. Fabrication of Near-Field Plasmonic Tip by Photoreduction for Strong Enhancement in Tip-Enhanced Raman Spectroscopy. *Appl. Phys. Express* **2012**, *5*, 052001.
12. Zhang, D.; Heinemeyer, U.; Stanciu, C.; Sackrow, M.; Braun, K.; Hennemann, L. E.; Wang, X.; Sholz, R.; Schreiber, F.; Meixner, A. J. Nanoscale Spectroscopic Imaging of Organic Semiconductors Films by Plasmon-Polariton Coupling. *Phys. Rev. Lett.* **2010**, *104*, 056601.
13. Ichimura, T.; Hayazawa, N.; Hashimoto, M.; Inouye, Y.; Kawata, S. Tip-Enhanced Coherent Anti-Stokes Raman Scattering for Vibrational Nanoimaging. *Phys. Rev. Lett.* **2004**, *92*, 220801.
14. Saito, Y.; Motohashi, M.; Hayazawa, N.; Iyoki, M.; Kawata, S. Nanoscale Characterization of Strained Silicon by Tip-Enhanced Raman Spectroscope in Reflection Mode. *Appl. Phys. Lett.* **2006**, *88*, 143109.
15. Yano, T.; Ichimura, T.; Kuwahara, S.; H'Dhili, F.; Uetsuki, K.; Okuno, Y.; Verma, P.; Kawata, S. Tip-Enhanced Nano-Raman Analytical Imaging of Locally-Induced Strain Distribution in Carbon Nanotubes. *Nat. Commun.* **2013**, *4*, 2592.
16. Okuno, Y.; Saito, Y.; Kawata, S.; Verma, P. Tip-Enhanced Raman Investigation of Extremely Localized Semiconductor-to-Metal Transition of a Carbon Nanotube. *Phys. Rev. Lett.* **2013**, *111*, 216101.
17. Anderson, N.; Hartschuh, A.; Novotny, L. Chirality Changes in Carbon Nanotubes Studied with Near-Field Raman Spectroscopy. *Nano Lett.* **2007**, *7*, 577–582.
18. Saito, Y.; Honda, M.; Moriguchi, Y.; Verma, P. Temporally Dynamic Photopolymerization of C_{60} Molecules in Single-Walled Carbon Nanotubes. *Phys. Rev. B* **2010**, *81*, 245416.
19. Cancado, L. G.; Hartschuh, A.; Novotny, L. Tip-Enhanced Raman Spectroscopy of Carbon Nanotubes. *J. Raman Spectrosc.* **2009**, *40*, 1420–1426.
20. Saito, Y.; Verma, P.; Masui, K.; Inouye, Y.; Kawata, S. Nano-Scale Analysis of Graphene Layers by Tip-Enhanced Near-Field Raman Spectroscopy. *J. Raman Spectrosc.* **2009**, *40*, 1430–1440.
21. Su, W.; Roy, D. Visualizing Graphene Edges Using Tip-Enhanced Raman Spectroscopy. *J. Vac. Sci. Technol., B: Microelectron. Nanometer Struct.--Process., Meas., Phenom.* **2013**, *31*, 041808.

22. Ossikovski, R.; Nguyen, Q.; Picardi, G. Simple Model for the Polarization Effects in Tip-Enhanced Raman Spectroscopy. *Phys. Rev. B* **2007**, *75*, 045412.
23. Mehtani, D.; Lee, N.; Hartschuh, R. D.; Kisliuk, A.; Foster, M. D.; Sokolov, A. P.; Maguire, J. F. Nano-Raman Spectroscopy with Side-Illumination Optics. *J. Raman Spectrosc.* **2005**, *36*, 1068–1075.
24. Blum, C.; Opilik, L.; Atkin, J. M.; Braun, K.; Kämmer, S. B.; Kravtsov, V.; Kumar, N.; Lemeshko, S.; Li, J. F.; Luszcz, K.; *et al*. Tip-Enhanced Raman Spectroscopy—An Interlaboratory Reproducibility and Comparison Study. *J. Raman Spectrosc.* **2013**, *45*, 22–31.
25. Curto, A. G.; Taminiau, T. H.; Volpe, G.; Kreuzer, M. P.; Quidant, R.; Hulst, N. F. Multipolar Radiation of Quantum Emitters with Nanowire Optical Antennas. *Nat. Commun.* **2013**, *4*, 1750.
26. Encina, E. R.; Coronado, E. A. Plasmonic Nanoantennas: Angular Scattering Properties of Multipole Resonances in Noble Metal Nanorods. *J. Phys. Chem. C* **2008**, *112*, 9586–9594.
27. Fourkas, J. T. Rapid Determination of the Three-Dimensional Orientation of Single Molecules. *Opt. Lett.* **2001**, *26*, 211–213.
28. Shegai, T.; Brian, B.; Miljkovic, V. D.; Kall, M. Angular Distribution of Surface-Enhanced Raman Scattering from Individual Au Nanoparticle Aggregation. *ACS Nano* **2011**, *5*, 2036–2041.
29. Böhmer, M.; Enderlein, J. Orientation Imaging of Single Molecules by Wide-Field Epifluorescence Microscopy. *J. Opt. Soc. Am. B* **2003**, *20*, 554–559.
30. Lieb, M. A.; Zavislan, J. M.; Novotny, L. Single-Molecule Orientations Determined by Direct Emission Pattern Imaging. *J. Opt. Soc. Am. B* **2004**, *21*, 1210–1215.
31. Taminiau, T. H.; Stefani, F. D.; Segerink, F. B.; Vanhulst, N. F. Optical Antennas Direct Single-Molecule Emission. *Nat. Photonics* **2008**, *2*, 234–237.
32. Kühn, S.; Mori, G.; Agio, M.; Sandoghdar, V. Modification of Single Molecule Fluorescence Close to a Nanostructure: Radiation Pattern, Spontaneous Emission and Quenching. *Mol. Phys.* **2008**, *106*, 893–908.
33. Huang, C.; Bouhelier, A.; Francs, G. C.; Bruyant, A.; Guenot, A.; Finot, E.; Weeber, J. C.; Dereux, A. Gain, Detuning and Radiation Patterns of Nanoparticle Optical Antennas. *Phys. Rev. B* **2008**, *78*, 155407.
34. Böhmler, M.; Hartmann, N.; Georgi, C.; Hennrich, F.; Green, A. A.; Hersam, M. C.; Hartschuh, A. Enhancing and Redirecting Carbon Nanotube Photoluminescence by an Optical Antenna. *Opt. Express* **2010**, *18*, 16443.
35. Novotny, L.; Sanchez, E. J.; Xie, X. S. Near-Field Optical Imaging Using Metal Tips Illuminated by Higher-Order Hermite-Gaussian Beams. *Ultramicroscopy* **1998**, *71*, 21–29.
36. Patra, D.; Gregor, I.; Enderlein, J. Image Analysis of Defocused Single-Molecule Images for Three-Dimensional Molecule Orientation Studies. *J. Phys. Chem. A* **2004**, *108*, 6836–6841.
37. Saito, Y.; Hayazawa, N.; Kataura, H.; Murakami, T.; Tsukagoshi, K.; Inouye, Y.; Kawata, S. Polarization Measurements in Tip-Enhanced Raman Spectroscopy Applied to Single-Walled Carbon Nanotubes. *Chem. Phys. Lett.* **2005**, *410*, 136–141.
38. Saito, Y.; Verma, P. Polarization Controlled Raman Microscopy and Nanoscopy. *J. Phys. Chem. Lett.* **2012**, *3*, 1295–1300.
39. Jorio, A.; Filho, A. G. S.; Brar, V. W.; Swan, A. K.; Unlu, M. S.; Goldberg, B. B.; Righi, A.; Hafner, J. H.; Lieber, C. M.; Saito, R.; *et al*. Polarized Resonant Raman Study of Isolated Single-Wall Carbon Nanotubes: Symmetry Selection Rules, Dipolar and Multipolar Antenna Effects. *Phys. Rev. B* **2002**, *65*, 121402.
40. Mark, I.; Stockman. Electromagnetic Theory of SERS. In *Surface-Enhanced Raman Scattering*; Kneipp, K.; Moskovits, M.; Kneipp, H., Eds.; Springer: Berlin, 2006; pp 47—65.
41. Itoh, T.; Yoshida, K.; Biju, V.; Kikkawa, Y.; Ishikawa, M.; Ozaki, Y. Second Enhancement in Surface-Enhanced Resonance Raman Scattering Revealed by an Analysis of Anti-Stokes and Stokes Raman Spectra. *Phys. Rev. B* **2007**, *76*, 085405.
42. Cancado, L. G.; Jorio, A.; Ismach, A.; Joselevich, E.; Hartschuh, A.; Novotny, L. Mechanism of Near-Field Raman Enhancement in One-Dimensional Systems. *Phys. Rev. Lett.* **2009**, *103*, 186101.
43. Larsen, R. E.; Metiu, H. Resolution and Polarization in Apertureless Near-Field Microscopy. *J. Chem. Phys.* **2001**, *114*, 6851.
44. Hartschuh, A.; Sanchez, E. J.; Xie, X. S.; Novotny, L. High-Resolution Near-Field Raman Microscopy of Single-Walled Carbon Nanotubes. *Phys. Rev. Lett.* **2003**, *90*, 095503.
45. Hayazawa, N.; Inouye, Y.; Sekkat, Z.; Kawata, S. Near-Field Raman Imaging of Organic Molecules by an Apertureless Metallic Probe Scanning Optical Microscope. *J. Chem. Phys.* **2002**, *117*, 1296–1301.
46. Hayazawa, N.; Yanob, T.; Kawata, S. Highly Reproducible Tip-Enhanced Raman Scattering Using an Oxidized and Metallized Silicon Cantilever Tip as a Tool for Everyone. *J. Raman Spectrosc.* **2012**, *43*, 1177–1182.
47. Richards, B.; Wolf, E. Electromagnetic Diffraction in Optical Systems. II. Structure of the Image Field in an Aplanatic System. *Proc. R. Soc. London, Ser. A* **1959**, *253*, 358–379.
48. Turrell, G. Analysis of Polarization Measurements in Raman Microspectroscopy. *J. Raman Spectrosc.* **1984**, *15*, 103–108.